Novel Synthesis of the TiO$_2$(B) Multilayer Templated Films

Jan Procházka,*,† Ladislav Kavan,† Markéta Zukalová,† Otakar Frank,† Martin Kalbáč,†
Arnošt Zukal,† Mariana Klementová,‡ Dina Carbone,§ and Michael Graetzel$^{||}$

*J. Heyrovsky Institute of Physical Chemistry, v.v.i, Academy of Sciences of the Czech Republic, Dolejškova
3, CZ-18223-Prague 8, Czech Republic, Institute of Inorganic Chemistry, v.v.i., Academy of Sciences of
the Czech Republic, CZ-250 68 Rez near Prague, Czech Republic, ESRF Grenoble, 38043 Grenoble
Cedex, France, and Laboratory of Photonics and Interfaces, Institute of Chemical Sciences and
Engineering, Swiss Federal Institute of Technology, CH-1015 Lausanne, Switzerland*

TiO$_2$(B) mesoporous thin films were grown in two steps on the F-doped SnO$_2$ conductive glass substrates. In the first step, a small amount of H$_3$PO$_4$, corresponding to 0.15−0.375 wt % P on TiO$_2$ basis, was introduced into concentrated HCl which was subsequently used for hydrolysis of titanium ethoxide. The hydrolyzed colloidal TiO$_2$ suspension was further mixed with a 1-butanol solution of the amphiphilic triblock copolymer Pluronic P123. The obtained precursor mixture was used for dip coating of FTO substrates. To achieve over 1 μm thick films, dip coating (followed by a thermal treatment at 350 °C/2 h) was repeated several times to produce multilayer films. The films consisted of amorphous TiO$_2$ with small amounts of anatase and TiO$_2$(B). The amorphous part was converted into the TiO$_2$(B) in a simple firing step at 500−550 °C. The formation of TiO$_2$(B) phase was accompanied by a significant increase of the film thickness. The films demonstrated unique behavior during the electrochemical lithium insertion that would qualify them for fast battery or electrochromic smart window applications. The efficiency of multiphase TiO$_2$ films in dye sensitized solar cells depends on the composition of individual films: it increases in the series: anatase/ amorphous TiO$_2$ < anatase/TiO$_2$(B) < anatase.

1. Introduction

TiO$_2$(B) fiberlike crystals exhibited a number of promising properties applicable in photocatalysis[1−3] and Li-ion batteries.[4−8] Unfortunately, the microcrystalline fiber morphology of TiO$_2$(B) synthesized from titanates limits the use of this material in certain applications. In this work, we introduce a novel synthesis producing mesoporous TiO$_2$(B) films on a conductive support with unique electrochemical characteristics and ordered crystal nanostructure.

TiO$_2$(B) is a metastable monoclinic modification of titanium dioxide. TiO$_2$(B) was first observed in 1980 by Marchand et al.[9,10] in a material prepared from layered potassium titanate K$_2$Ti$_4$O$_9$ via K$^+$/H$^+$ ion exchange followed

by calcinations.[9−11] Since then, TiO$_2$(B) has been reported several times,[2,12−15] and Banfield et al.[16] have first found TiO$_2$(B) in nature. Monoclinic TiO$_2$(B) crystallizes in the space group *C*2/*m* with the lattice parameters: $a = 1.21787$ nm, $b = 0.37412$ nm, $c = 0.65249$ nm, $\beta = 107.054°$.[17] The structure is isotypic to that of Na$_x$TiO$_2$ (bronze), $x = 0.2$, where the name "TiO$_2$(B)" comes from.[4,18] The specific gravity of TiO$_2$(B) is 3.64−3.76 g/cm.[3] TiO$_2$(B) is an n-type semiconductor with a band gap of 3−3.22 eV.[8,13,19] Consequently, TiO$_2$(B) shows photoanodic[19] and photocatalytic[2,3,13] activity in UV light. TiO$_2$(B) also accommodates Li$^+$ to form Li$_x$TiO$_2$(B). The insertion coefficient x was found 0.75−0.85 by the reaction with *n*-butyl-lithium, and $x \approx 0.5$−0.75 by electrochemistry.[4−6,10,20] High electrochemical capacity ($x = 0.82$, i.e., 275 mA h g^{-1}) was reported for hydrothermally

* Corresponding author. E-mail: jan.prochazka@jh-inst.cas.cz.
† J. Heyrovsky Institute of Physical Chemistry, v.v.i, Academy of Sciences of the Czech Republic.
‡ Institute of Inorganic Chemistry, v.v.i., Academy of Sciences of the Czech Republic.
§ ESRF Grenoble.
$^{||}$ Swiss Federal Institute of Technology.

(1) Wang, Q.; Wen, Z.; Li, J. *Adv. Funct. Mater.* **2006**, *16*, 2141.
(2) Yin, S.; Fujishiro, Y.; Wu, J.; Aki, M.; Sato, T. *J. Mater. Proc. Technol.* **2003**, *137*, 45.
(3) Zukalova, M.; Kalbac, M.; Kavan, L.; Exnar, I.; Haeger, A.; Grätzel, M. *Prog. Solid State Chem.* **2005**, *33*, 253.
(4) Zachau-Christiansen, B.; West, K.; Jacobsen, T.; Skaarup, S. *Solid State Ionics* **1992**, *53−56*, 364.
(5) Kawamura, H.; Muranishi, Y.; Miura, T.; Kishi, T. *Denki Kagaku* **1991**, *59*, 766.
(6) Zachau-Christiansen, B.; West, K.; Jacobsen, T.; Atlung, S. *Solid State Ionics* **1988**, *28−30*, 1176.
(7) Armstrong, A. R.; Armstrong, G.; Canales, J.; Bruce, P. G. *Angew. Chem., Int. Ed.* **2004**, *43*, 2286.
(8) Nuspl, G.; Yoshizawa, K.; Yamabe, T. *J. Mater. Chem.* **1997**, *7*, 2529.
(9) Marchand, R.; Brohan, L.; Tournoux, M. *Mater. Res. Bull.* **1980**, *15*, 1129.
(10) Tournoux, M.; Marchand, R.; Brohan, L. *Prog. Solid St. Chem.* **1986**, *17*, 33.
(11) Brohan, L.; Verbaere, A.; Tournoux, M.; Demazeau, G. *Mater. Res. Bull.* **1982**, *17*, 355.
(12) Yin, S.; Uchida, S.; Fujishiro, Y.; Aki, M.; Sato, H. *J. Mater. Chem.* **1999**, *9*, 1191.
(13) Yin, S.; Wu, J.; Aki, M.; Sato, T *Int. J. Inorg. Mat* **2000**, *2*, 325.
(14) Wallenberg, L. R.; Sanati, M.; Andersson, A. *Microsc. Microanal. Microstruct.* **1990**, *1*, 357.
(15) Kogure, T.; Umezawa, T.; Kotani, Y.; Matsuda, A.; Tatsumisago, M.; Minami, T. *J. Am. Ceram. Soc.* **1999**, *82*, 3248.
(16) Banfield, J.; Veblen, D.; Smith, D. *Am. Mineral.* **1991**, *76*, 343.
(17) Feist, T. P.; Davies, P. K. *J. Solid State Chem.* **1992**, *101*, 275.
(18) Theobald, F.; Cabala, R.; Bernard, J. *J. Solid State Chem.* **1975**, *17*, 431.
(19) Betz, G.; Tributsch, H.; Marchand, R. *J. Appl. Electrochem.* **1984**, *14*, 315.
(20) Brohan, L.; Marchand, R. *Solid State Ionics* **1983**, *9−10*, 419.

grown $TiO_2(B)$ nanowires.[7,21,22] These nanowires also showed promising results in a new hybrid supercapacitor.[23]

Zukalova et al.[24] described preparation and characterization of the phase-pure micrometer-sized powder materials. The relatively complicated technique producing $TiO_2(B)$ powder with fiber morphology starts from the solid state synthesis of cesium titanate, followed by Cs^+/H^+ exchange and calcination. Preparation of optically transparent thin films made of this phase pure material was difficult because of the poor stability of $TiO_2(B)$ and other limitations such as light scattering factor due to the large particle size.

Zukalova et al.[24] have also reported on the somewhat unexpected occurrence of $TiO_2(B)$ in mesoporous Pluronic (P-123)-templated TiO_2 structures. This phase was overlooked in previous reports on Pluronic-templated titania,[25−29] but was later confirmed by Fattkhova-Rohlfing et al.[30] in similar TiO_2 materials made by supramolecular templating. The organized mesoporous titania films find promising applications in photovoltaics[31−35] and photocatalysis (for a recent review see ref 36). The growth of the $TiO_2(B)$ phase in templated TiO_2 films is reminiscent of the unanticipated detection of $TiO_2(B)$ during calcination of sol−gel-derived $SiO_2−TiO_2$ amorphous film at 900 °C.[15] However, the conditions controlling the formation of $TiO_2(B)$/anatase and/or other phases in the mesoporous films are not clearly understood yet.

The beneficial impact of the phosphorus-doped TiO_2 powders on photocatalysis was previously reported by Yu et al.[37] However, the authors dealt only with powders and did not observe any formation of $TiO_2(B)$ crystals. Here we show that the phosphorus doping is also useful for stabilizing the $TiO_2(B)$ fraction in thin films. The term 'doping' is used here, in accord with general practice, to denote titania materials containing heteroatom (P) but not showing any additional crystalline phases except TiO_2 by using the conventional methods of characterization of solids. However, as the structural localization of phosphorus in our material is unknown, this name need not mean 'true' (interstitial or substitutional) doping of semiconductors in a physical sense. Optically transparent mesoporous films containing high proportion of $TiO_2(B)$ were prepared in over 3 μm of thickness. The progress has been achieved through the modification of the sol−gel recipe[31,32,38] by adding phosphate to the precursor. To our best knowledge, the synthesis of mesoporous, predominantly $TiO_2(B)$ transparent films by means of phosphorus doping is reported here for the first time.

2. Experimental Section

2.1. Materials. The TiO_2 films were grown from a suspension made by the addition of 10.2 mL of concentrated HCl (37% Aldrich) to 14.4 g of titanium ethoxide (Aldrich) under vigorous stirring. Phosphorus doping was introduced into the suspension by addition of 0.235−0.6 mL of 85% H_3PO_4 (0.15−0.375 wt % P on a TiO_2 basis) to the concentrated HCl. Separately, a 5.0 g of block copolymer Pluronic P123 $[OH(CH_2CH_2O)_{20}(CH_2CH(CH_3)O)_{70}(CH_2CH_2O)_{20}H]$ from Aldrich was dissolved in 56 mL of 1-butanol (Aldrich) and added to the $HCl/Ti(EtO)_4/H_3PO_4$ suspension. This suspension was aged by stirring at ambient temperature for at least 3 h. The films were deposited by dip coating (withdrawal rate of 0.8 mm/s) onto 2 × 7 cm^2 sized slides of F-doped SnO_2 conductive glass (TEC 8 from Libbey-Owens-Ford, 8 Ω/square; further abbreviated FTO). For this purpose, we have used a homemade setup for vibration-free dip-coating. The apparatus consisted of a hydraulic piston, which was operated by a precision pump (KD Scientific, USA). Optionally, the layers were aged at 75% relative humidity and 24−25 °C for 24 h. Subsequently, the layer was calcined in air at 350 °C for 2 h (heating rate: 1 °C/min). Thicker multilayer films were manufactured by repeating the procedure up to ten times. In the final step, these films were fired at temperatures of 500−550 °C for 1−3 h to promote the $TiO_2(B)$ crystal phase development. Different temperature ramps did not have any noticeable impact on the crystal phase formation. Lowering the content of phosphorus led to higher portion of anatase in the $TiO_2(B)$ matrix. Anatase structures were prepared with no phosphorus added. For comparison, a standard sample of $TiO_2(B)$ powder was prepared from cesium titanate by following the synthetic protocol of ref 24.

All TiO_2 films were crack-free and optically transparent. The film thickness and TiO_2 surface area were linearly proportional to the number of layers. Considerable increase of the film thickness was observed during the final firing step above 500 °C. The forming of $TiO_2(B)$ was accompanied by swelling of the film more than 35% relative to the original thickness.

2.2. Characterization Methods. Adsorption isotherms of krypton at 77 K were measured with a Micromeritics ASAP 2020 instrument. Before the adsorption measurement, all samples were degassed at 523 K overnight. The BET surface areas were calculated using the data in the range of relative pressure p/p_0 from 0.05 to 0.25. Following the usual practice, the saturation vapor pressure p_0 of the supercooled liquid krypton and the atomic cross-sectional area of 0.21 nm^2 were used. The specific surface area is expressed by the roughness factor (RF), which is the physical surface area of

(21) Armstrong, A. R.; Armstrong, G.; Canales, J.; Bruce, P. G. *J. Power Sources* **2005**, *146*, 501.
(22) Armstrong, G.; Armstrong, A. R.; Canales, J.; Bruce, P. G. *Electrochem. Solid-State Lett.* **2006**, *9*, A139−A143.
(23) Wang, Q.; Wen, Z.; Li, J. *Adv. Funct. Mater.* **2006**, *16*, 2141.
(24) Zukalova, M.; Kalbac, M.; Kavan, L.; Exnar, I.; Grätzel, M. *Chem. Mater.* **2005**, *17*, 1248.
(25) Kavan, L.; Rathousky, J.; Grätzel, M.; Shklover, V.; Zukal, A. *J. Phys. Chem. B* **2000**, *104*, 12012.
(26) Kavan, L.; Rathousky, J.; Grätzel, M.; Shklover, V.; Zukal, A *Microporous Mesoporous Mater.* **2001**, *44−45*, 653.
(27) Yang, P.; Zhao, D.; Margolese, D. I.; Chmelka, B. F.; Stucky, G. D. *Chem. Mater.* **1999**, *11*, 2813.
(28) Choi, S. Y.; Mamak, M.; Coombs, N.; Chopra, N.; Ozin, G. A. *Adv. Funct. Mater.* **2004**, *14*, 335.
(29) Crepaldi, E. L.; Soler-Illia, G.J.A.A.; Grosso, D.; Cagnol, F.; Ribot, F.; Sanchez, C. *J. Am. Chem. Soc.* **2003**, *125*, 9770.
(30) Fattakhova-Rohlfing, D.; Wark, M.; Brezesinski, T.; Smarsly, B. M.; Rathousky, J. *Adv. Funct. Mater.* **2007**, *17*, 123.
(31) Zukalova, M.; Zukal, A.; Kavan, L.; Nazeeruddin, M. K.; Liska, P.; Grätzel, M. *Nano Lett.* **2005**, *5*, 1789.
(32) Zukalova, M.; Prochazka, J.; Zukal, A.; Yum, J. H.; Kavan, L. *Inorg. Chim. Acta* **2008**, *361*, 656.
(33) Lancelle-Beltran, E.; Prene, P.; Boscher, C.; Belleville, P.; Buvat, P.; Lambert, S.; Guillet, F.; Boissiere, C.; Grosso, D.; Sanchez, C. *Chem. Mater.* **2006**, *18*, 6152.
(34) Lancelle-Beltran, P.; Prene, P.; Boscher, C.; Belleville, P.; Buvat, P.; Sanchez, C. *Adv. Mater.* **2006**, *18*, 2579.
(35) Lancelle-Beltran, E.; Prene, P.; Boscher, C.; Belleville, P.; Buvat, P.; Lambert, S.; Guillet, F.; Marcel, C.; Sanchez, C. *Eur. J. Inorg. Chem.* **2008**, 903.
(36) Sanchez, C.; Boissiere, C.; Grosso, D.; Laberty, Ch.; Nicole, L. *Chem. Mater.* **2008**, *20*, 682.
(37) Yu, J. C.; Zhang, L.; Zheng, Z.; Zhao, J. *Chem. Mater.* **2003**, *15*, 2280.
(38) Prochazka, J.; Kavan, L.; Shklover, V.; Zukalova, M.; Frank, O.; Kalbac, M.; Zukal, A.; Pelouchova, H.; Janda, P.; Mocek, K.; Klementova, M.; Carbonne, D. *Chem. Mater.* **2008**, *20*, 2985.

Table 1. GISAXS Analysis of a Five-Layer TiO₂(B) Film[a]

GISAXS scan angle (deg)	peak 1, 2θ/D (deg/nm)	peak 2, 2θ/D, (deg/nm)	peak 3, (2θ/D (deg/nm)	peak 4, 2θ/D (deg/nm)	peak 5, 2θ/D (deg/nm)	peak 6, 2θ/D (deg/nm)
0.1	0.20/**35**	0.47/**15**	0.80/**9**	0.97/**7**	1.50/**5**	1.60/**4**
0.2	A	0.43/**16**	0.83/**9**	0.87/**8**	0.93/**8**	1.53/**5**
0.3	A	0.40/**18**	0.87/**8**	1.20/**6**	1.40/**5**	*
0.6	A	0.37/**19**	0.77/**9**	0.93/**8**	1.23/**6**	1.33/**5**

[a] The penetration depth of the beam increases with the scan angle from 0.1 to 0.6°. Parameters of each peak indicate the angle of the event occurrence and the corresponding size of the event. Note: A = the peak is absent under the surface; * = intensity at the detection limit.

Figure 1. Development of the TiO₂ surface area (circles) and the film thickness (crosses) with the number of layers during the first preparation step at 350 °C. Full circles are for P-doped and empty circles are for undoped TiO₂ films. Crosses represent film thickness for both doped and undoped films.

the TiO₂ electrode divided by its geometric area. The film thicknesses were measured by alpha-step profilometer, Tencor Instruments. Scanning electron microscopy (SEM) images were acquired at Hitachi FE SEM S-4800 microscope. Transmission electron microscopy (TEM) studies was carried out on a JEOL JEM 3010 microscope operating at 300 kV (LaB₆ cathode, point resolution 1.7 Å) with an EDX (energy-dispersive X-ray) detector attached. Images were recorded by a CCD camera with resolution of 1024 × 1024 pixels using the Digital Micrograph software package. Powder samples were dispersed in ethanol and the suspension was sonicated for 10 min. A drop of very dilute suspension was placed on a carbon-coated grid and allowed to evaporate at ambient temperature. Electron diffraction patterns were evaluated using the Process diffraction software package.[39] Raman spectra were excited by an Ar⁺ laser at 2.41 eV (Innova 305, Coherent) and recorded on a T-64000 spectrometer (Instruments, SA).

The prepared films were also tested in dye-sensitized solar cells.[31,32] To this purpose, the films were modified by adsorption of (4,4-dicarboxy-2,2-bipyridine)(4,4′-di-(2-(3,6-dimethoxyphe-nyl)ethenyl)-2,2′-bipyridine) *cis*-dithiocyanato ruthenium(II), further abbreviated as N-945.[31] The sensitized films were further tested in photoelectrochemical cells, as described elsewhere.[31] The amount of adsorbed N-945 dye was determined as follows. The N-945 sensitized electrode was dipped into 5.00 mL of 1 × 10⁻⁴ M NH₄OH. The mixture was stirred, until complete desorption of the dye into the liquid took place. The resulting dye solution was analyzed spectrophotometrically in a 1.00 cm quartz optical cell. The concentration was calculated using the extinction coefficient 18600 M⁻¹ cm⁻¹ at λ = 545 nm.

Grazing incidence small-angle X-ray scattering (GISAXS) measurements were carried out at the ID1 unit of the Grenoble ESRF facility using 10 keV beam. Position sensitive detector was placed along the direction perpendicular to the sample surface, so

(39) Labar, J. L. *Ultramicroscopy* **2005**, *103*, 237.

that during GISAXS acquisition we could acquire a Q_x–Q_z map in one scan, or integrate the intensity on the whole detector (about 2°). Generally the GISAXS scans are shown in Q space. This can be done using the simple relations

$$Q_x = 2\pi\sin\theta/\lambda\,[1/nm] \text{ and } O_z = 2\pi\sin\theta_{PSD}/\lambda\,[1/nm] \quad (1)$$

λ is the radiation wavelength (1.2397 Å), θ is the diffraction angle, and θ_{PSD} is the angle along the PSD detector. In this way it is straightforward to calculate the average particle–particle distance

$$D = 2\pi/Q_{max} \quad (2)$$

where Q_{max} is the position of the first ordering peak in Q_x. Relative density of the film was determined from the critical angle values of the reflectivity scans. The beam penetrated more than one layer at 0.4 degrees indicating a very porous structure. Exclusion method was used to associate the peaks on the GISAXS scans with the particle size values and different types of pore sizes (Table 1). Reference data for this exclusion were obtained by the analytical methods described in this section. The coherent domain size of TiO₂(B) particles was also calculated from diffraction patterns of wide-angle X-ray scattering (WAXS) using the Scherrer equation.

Electrochemical lithium insertion was studied by cyclic volta-mmetry using the Autolab PGSTAT 30 (Ecochemie) potentiostat controlled by a GPES-4 software. The reference and auxiliary electrodes were Li metal. The potentials are referred to the Li/Li⁺ (1M) reference electrode. The electrolyte solution was 1 M LiPF₆ + ethylene carbonate/dimethyl carbonate (EC/DMC; 1/1 by mass). All operations were done under argon in a glovebox.

For photoelectrochemical tests, the dye-coated TiO₂ film was illuminated through the conducting glass support. The light source was a 450 W xenon lamp that was focused to give light power of 1000 W/m², the equivalent of one Sun at AM 1.5, at the surface of test cell. The spectral output of the lamp was matched in the wavelength region of 340–800 nm with the aid of a Schott KG-5 sunlight filter. The applied potential and cell current were measured using a Keithley model 2400 digital source meter.

3. Results and Discussion

3.1. Step 1: Multilayer Films Consisting of Amorphous TiO₂. The surface area and thickness of the amorphous multilayer films prepared via the phosphorus doping protocol show a linear increase with the number of layers. (By the term "amorphous" is here meant a TiO₂ material, showing just short-range ordering that is nonde-tectable by X-ray diffraction, Raman spectroscopy, or Li-insertion electrochemistry. Note that our samples may contain small portion of anatase and TiO₂(B) in the amorphous matrix.) In contrast to the undoped (P-free) films, no sign of disproportional sintering during the deposition of each layer was observed.[32,38] Figure 1 shows that the surface area (the film's roughness factor-RF) increases linearly with the number of layers in the P-doped film, whereas RF reaches a
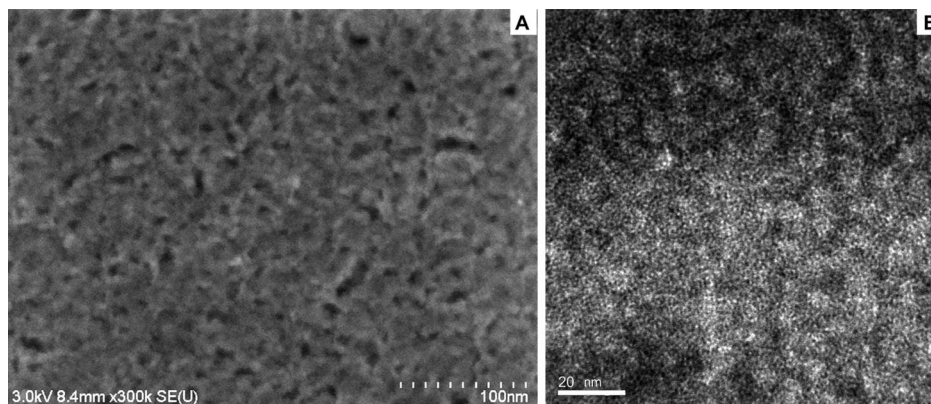
Figure 2. Electron micrographs of the P123-templated phosphorus-doped amorphous TiO₂ structure before the final firing step: (A) SEM picture of the surface, (B) HR-TEM of the bulk.
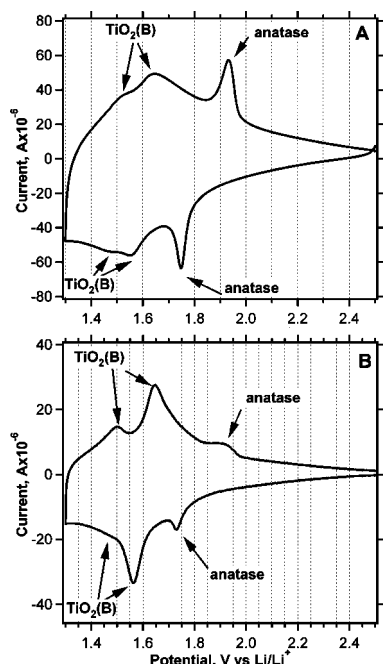

Figure 3. Cyclic voltammograms of Li⁺ insertion into TiO₂ at 0.1 mV/s show (A) amorphous character of a 4-layer film (before the final thermal treatment) also containing anatase and TiO₂(B), (B) pronounced crystallization of TiO₂(B) in the 1-layer film after the final thermal treatment at 530 °C/2 h.

TEM image of the amorphous film is in Figure 2B. The individual particles of the TiO₂ are mostly spherical with the typical particle size around 3 nm. The HR-TEM indicates the dominant amorphous character of TiO₂.

Cyclic voltammetry of Li insertion is an effective method for phase analysis of TiO₂.[24,30,38] Figure 3A shows the dominating presence of amorphous TiO₂ with small amounts of TiO₂(B) and anatase (under 30%) in the P-doped film, before the final high-temperature calcination. The amorphous material contains 0.15 wt % of phosphorus, and it converts into the TiO₂(B) as the main phase during the final firing step at 530 °C for 2 h (Figure 3B). The fraction of anatase already formed in any synthesis step is always present in the final material. On the basis of the integration of the characteristic peaks on the cyclic voltammograms, the content of anatase ranges from 5 to 30%.

3.2. Step 2: Conversion of the Amorphous TiO₂ Multilayer Films into TiO₂(B) Particle Network. Upon the final thermal processing step, firing at 450 to 550 °C for 30 min to 8 h, the amorphous TiO₂ particles fuse and crystallize into TiO₂(B). Figure 4 shows SEM images of the fired sample. The transformation of the P-doped amorphous TiO₂ into TiO₂(B) mimics the phase development in pristine amorphous TiO₂ reported by Zukalova et al.[24] Although the impact of phosphorus doping is not yet fully understood, it seems to promote the crystallization of TiO₂(B) in addition to the film surface area linear increase during subsequent layer deposition. The aspect ratio of TiO₂(B) nanoparticles made by the phosphorus-doping synthesis differs from that in the micronmeter-sized crystals made by the solid-state synthesis from cesium titanate.[24] Although the long needles of the phase-pure TiO₂(B) material synthesized from cesium titanate (see Experimental Section) grow several micrometers along the *b*-axis (Figure 5), the particle growth of P-doped TiO₂(B) is hindered in this direction. The aspect ratio of the nanoparticles along the *a* and *c* axes is approximately 2, determined from TEM.

Figure 6 shows Raman spectra of phase pure anatase (curve A) and phase pure TiO₂(B) (curve C), compared to the spectrum of P-doped P123 templated thin film (curve B). By proper fitting, all bands belonging to anatase and TiO₂(B) can be found in curve B. The nonoverlapping

constant value above three layers in the undoped TiO₂ film. The latter conclusion reproduces our earlier data for undoped film,[32,38] and confirms that even phosphorus levels under 0.05 wt % P in TiO₂ cause explicit morphological stability of the multilayer film. Although the film thickness scales linearly with the number of layers, both for undoped[38] and doped films (Figure 1), the proportionality of roughness factor and number of layers is a novel issue specific for phosphorus doping only.

Figure 2A shows a SEM micrograph of the surface of the amorphous P-doped film. The partially "sealed" P123 micelle imprints demonstrate an analogy with the structure of anatase inverse opal,[38,40] although opals are macroporous materials, which is not the case in our mesoporous films. The average size of the P123 ex-micelle related pores is 15−20 nm. HR-

(40) Kavan, L.; Zukalova, M.; Kalbac, M.; Grätzel, M. *J. Electrochem. Soc.* **2004**, *151*, A1301−A1307.
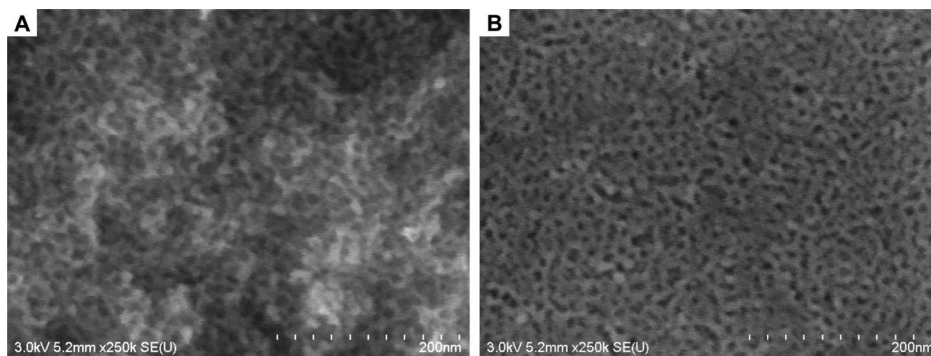
Figure 4. SEM picture of the P123 templated TiO_2(B) film made at 530 °C: (A) cross-sectional view, (B) surface view.
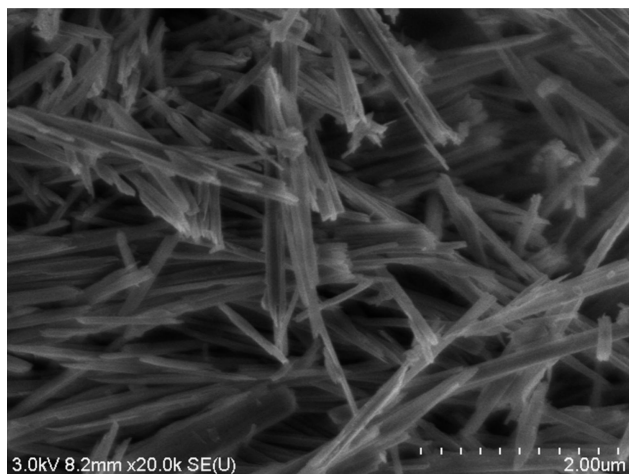

Figure 5. Micrometer-size needles of phase-pure TiO_2(B) made from cesium titanate. High aspect ratio in the *b*-axis direction is seen on the micrograph.
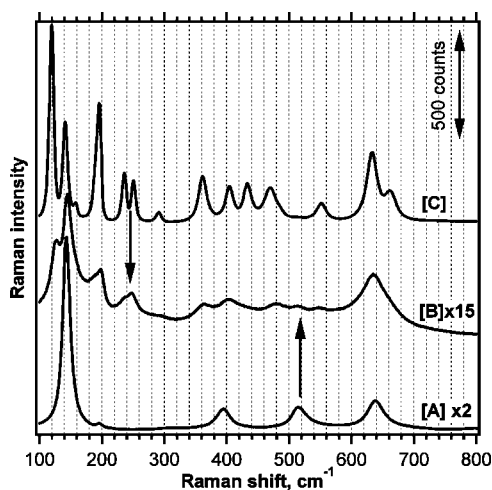

Figure 6. Raman spectra of the P123 templated mesoporous film containing TiO_2(B) (curve B) in comparison with the spectra of phase pure anatase (curve A) and phase pure TiO_2(B) powders (curve C). The arrows point to the nonoverlapping peaks differentiating both phases.

diagnostic bands (two bands around 250 cm^{-1} for TiO_2(B) and the band at 515 cm^{-1} for anatase) are marked with arrows. TEM analysis in Figure 7 reveals porous character of the P123 templated structure. Pores 15−20 nm in size are imprints of the micelles of the P123 copolymer.[38] This structure is analogous to the inverse opal structure,[40] but on a nanometer scale. The orientation of the individual TiO_2(B)

crystals is random. Figure 8 shows the diffraction pattern of the film, indicating almost phase pure TiO_2(B).

The TiO_2 film swells of about 35−40% during the crystallization process into TiO_2(B) upon the thermal treatment above 500 °C. The thickness of the five-layer film increases from 1.3 to 1.8 μm after the final calcination step. This effect is most likely associated with changes in geometry of the particles during the fusion. The 3 nm spherical particles of the amorphous TiO_2 transform into approximately 4×9 nm oval needles of TiO_2(B). During the crystallization process, the roughness factor of the film was reduced from 840 to 450 (TiO_2 specific surface area was approximately 200 m^2/g).

The TiO_2 film overall density, morphology, and crystal phase were determined by GISAXS. The measured values are arranged in Table 1. The corresponding analyses are in Figures 9 and 10. The critical reflective angle values indicate the overall density of TiO_2 films to be around 1.3 g/cm^3, which means approximately 70% porosity. The amorphous TiO_2 structure is slightly denser with the critical angle of 0.15° compared to 0.132° of TiO_2(B) swollen film. The maximal reflection of a TiO_2 dense layer is at 0.165°. The diffraction scans (WAXS) at the scan angle equal, above and below the critical angle show the diffraction patterns of the film with the increasing penetration depth (Figure 9). Scherrer calculations of the peak around 11 deg at different penetration depth provided consistently the particle size of TiO_2(B) to be 4 nm. The domain size of traces of anatase was calculated as 8 nm.

The statistical maxima of GISAXS scans (Figure 10) are shown in Table 1. The peak at 35 nm is associated with surface defects. P123 ex-micelle porosity most likely belongs to the peak at 15−19 nm. The peak at 35 nm is only present in the surface scan. The 35 nm event does not exist under the surface. Cracks and defects of this average size were observed on the surface by the SEM. The event at 15 nm is clearly associated with the size of the artificial porosity incorporated into the structure through P123 copolymer micelles. The value corresponds well with the other measurements of the undoped TiO_2[38] structure and agrees with the SEM and TEM data. Similar to other mesoporous structures, there is a denser crust on the surface of the film up to tens of nanometers thick. No densification of the bottom layers was observed.
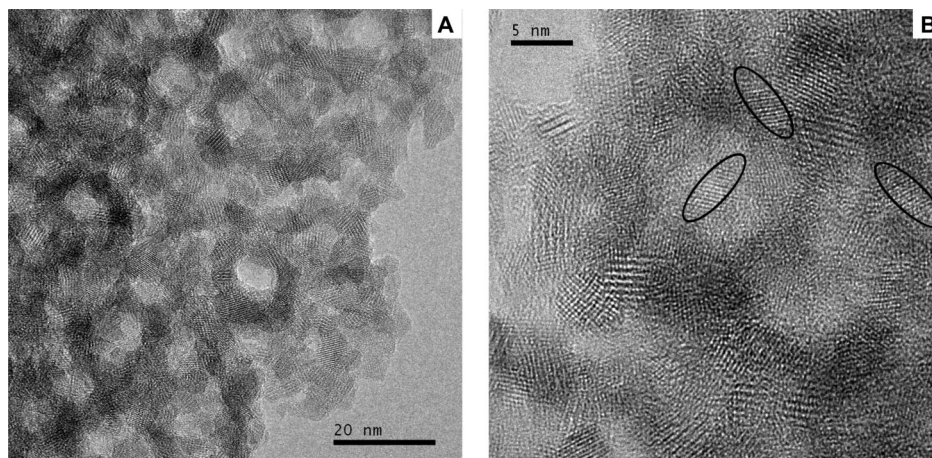
Figure 7. HR-TEM characterization: (A) "inverse opal" morphology of P123 templated TiO$_2$(B) structure, (B) random orientation of the TiO$_2$(B) individual crystals.
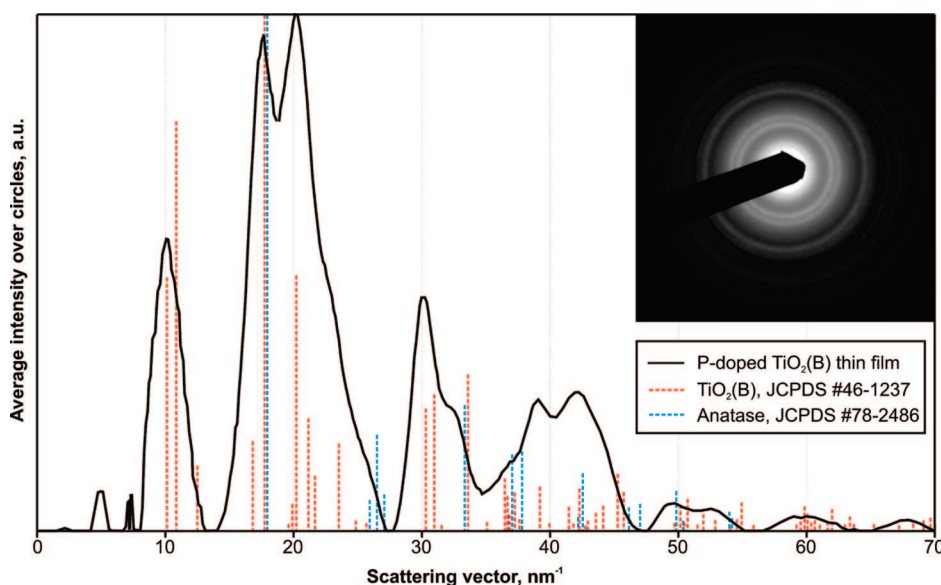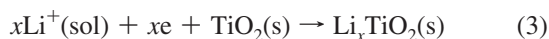

Figure 8. TEM characterization and selected area electron diffraction pattern of the TiO$_2$(B) film.

Several peaks in the 4−9 nm range are almost undistinguishable. Some might have been associated with the size and shape of the primary particles, while the rest reflect the interparticle porosity. Dimensions of the primary particles are approximately 4 × 9 nm.

3.3. Properties of the Multilayer TiO$_2$(B) Films. The multilayer TiO$_2$(B) films are optically transparent up to 5 μm of thickness. The structure shows some interesting properties that were already found in the coarse TiO$_2$(B).[24] The previously observed fast insertion and extraction of lithium is even faster with the small particle size. The lithium insertion and extraction

$$x\text{Li}^+(\text{sol}) + x\text{e} + \text{TiO}_2(\text{s}) \rightarrow \text{Li}_x\text{TiO}_2(\text{s}) \qquad (3)$$

is accompanied by an intensive color change. Complete charge and discharge occur in seconds and the coloring/discoloring effect is practically instant upon the potential switching (Figure 11A). The reversibility of charge and discharge and the cycle stability are very good. The charge reversibility is demon-

strated by overlapping curves in Figure 11B. When cycled between 1.2 and 2.5 V, 90 s per cycle, the capacity dropped by only 20% after 800 full charge/discharge cycles. The lithium insertion formal potential of 1.5 V and the fast charge/discharge characteristics of TiO$_2$(B) are similar to those of nanoparticles of lithium titanate;[41] however, TiO$_2$(B) films possess very good mechanical properties and optical transparency that are not common for lithium titanate films.

The five-layer transparent film consisting of TiO$_2$(B) with approximately 30% anatase was used for a test in the dye-sensitized solar cell (DSC). The content of anatase was determined electrochemically as in ref.[30] Three TiO$_2$ electrodes were used to determine the TiO$_2$(B) activity in the DSC device. Figure 12 shows photocurrent−voltage curves of the cells at 1 Sun light intensity. The first electrode consisted of approximately 30% of anatase and 70% of

(41) Kavan, L.; Prochazka, J.; Spitler, T. M.; Kalbac, M.; Zukalova, M.; Drezen, T.; Grätzel, M. *J. Electrochem. Soc.* **2003**, *150*, A1000−A1007.
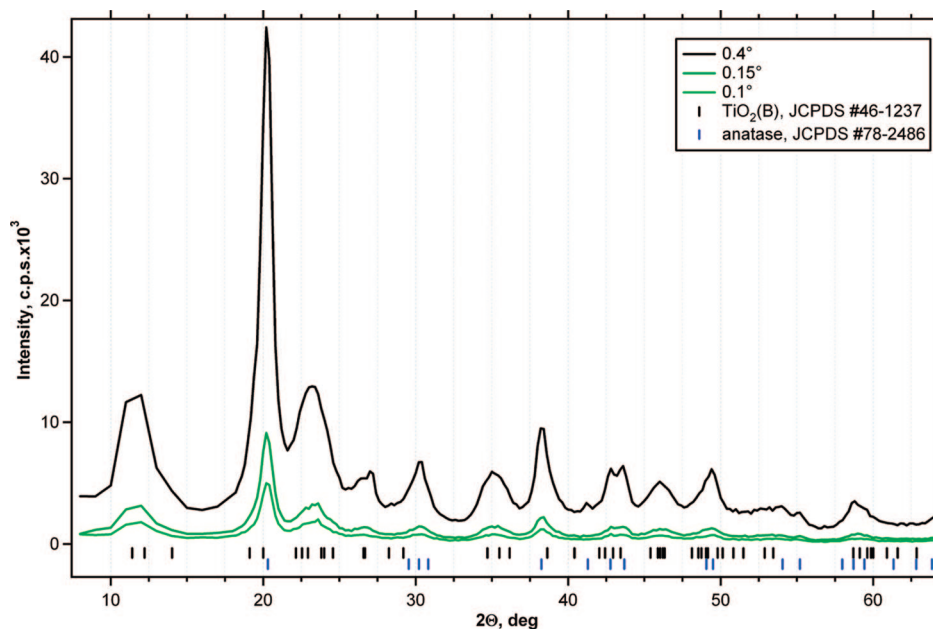
Figure 9. WAXS diffraction patterns of five-layer film thermally post-treated at 530 °C/2 h.

amorphous TiO_2. The sample was originating from the first stage of the synthesis. The second electrode was the same sample calcined at 530 °C giving a similar anatase ratio of 30% and 70% of $TiO_2(B)$. The last sample was an electrode made of the phase pure anatase (no phosphorus doping). The electrodes were sensitized by a monolayer of the N-945 dye deposited on TiO_2 from acetonitrile + *t*-butanol solution (1/1, w/w) solution. The dye coverage of all samples was comparable. The solar conversion efficiency η of the first device was less than 0.5% (30% of anatase in the amorphous TiO_2). This sample was practically inactive, while after calcination the performance increased to 2.2% (30% of anatase in $TiO_2(B)$). The solar conversion efficiency of the pure anatase film was 4.5%. The surface areas of the $TiO_2(B)$ and anatase electrodes were almost the same, with a roughness factor around 420.

Because of the low anatase content in the P-doped TiO_2 thin films the nanoparticles of anatase were probably not interconnected. In fact, they must have been separated by the $TiO_2(B)$ crystals. Our explanation of the relatively high solar efficiency of the $TiO_2(B)$/anatase blend is the electron conductivity of the dye-sensitized $TiO_2(B)$. The experiment indicates that $TiO_2(B)$ is not capable to collect electrons released by the dye upon illumination; however, once the electron has entered the $TiO_2(B)$ network, the structure is able to transport electrons in the same manner as the anatase TiO_2. Similar conclusions may be drawn from ref 42. The solar conversion efficiency of 2.2% is proportional to the expected activity of 30% of anatase present in the sample. Obviously, the randomly distributed anatase nanoparticles transmit the photoexcited electrons originating from the illuminated dye that are further transferred through the $TiO_2(B)$/anatase heterogeneous structure to the conductive FTO substrate. The $TiO_2(B)$ function may have allowed

the anatase to be fully active in the dye sensitized solar cell in contrast to the anatase in the amorphous TiO_2 matrix.

4. Conclusions

New synthesis of nanosized $TiO_2(B)$ based on phosphorus addition to the sol−gel precursor was developed. The phosphorus level was 0.15−0.375 wt % P on a TiO_2 basis. The synthesis conveniently allows manufacturing of thin films "in situ" on FTO conductive substrates. The mesoporous P123 templated $TiO_2(B)$ films consisting of 1−10 layers were up to 4 μm thick with high transparency in visible light. The overall film porosity was around 70% (1.3 g/cm³) with the $TiO_2(B)$ specific surface area of approximately 200 m²/g. The roughness factor of a five-layer film was typically around 420. The P123 ex-micelle pore size was between 15 and 20 nm. Crystal phase purity of $TiO_2(B)$ films was nearly 95%. On the basis of the electrochemical determination and other analyses, the phase purity was controllable in the range from 70 to 95% by the phosphorus content in combination with the final thermal treatment. Traces of TiO_2−anatase are stable and persist all steps of the preparation procedure. The average particle size of the anatase was 8 nm. Needles of $TiO_2(B)$ mostly 4 × 9 nm in size were organized in the walls (shells) around the P123 ex-micelles. No long-range organization of the pores or particles was observed.

The films showed fast lithium ion insertion/extraction at the formal potential of 1.5 V vs Li/Li⁺. The electrochemical cycling stability was good. After 800 complete lithium insertion and extraction cycles, the capacity drop was only 20%. The lithium accumulation was accompanied by a strong electrochromic effect. Coloring and discoloring of the film occurred instantly upon the potential switching. The color turned from transparent white into transparent dark blue.

On the basis of behavior of the film consisting of 70% $TiO_2(B)$ and 30% anatase in DSC, the dye-sensitized $TiO_2(B)$

(42) Asagoe, K.; Ngamsinlapasathian, S.; Suzuki, Y.; Yoshikawa, S. *Centr. Eur. J. Chem.* **2007**, *5*, 605.
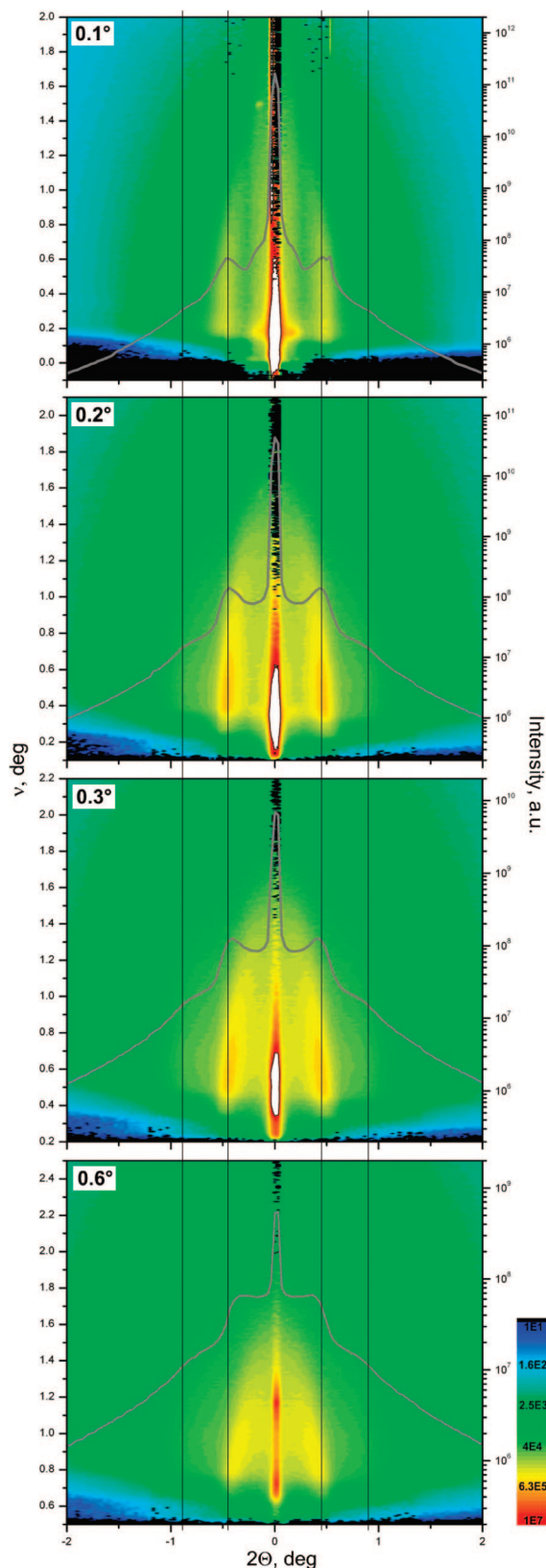
Figure 10. GISAXS detector maps at 0.1° (surface-low penetration depth), 0.2° (surface), 0.3° (penetrates 20−200 nm under the surface), and 0.6° (penetration depth several hundred nanometers). The maxima values are in Table 1. The curve shows the integral intensity.

is most likely capable of the electron transport, although the direct electron transfer from the Ru-bipyridine dye (N-945) into TiO$_2$(B) is unlikely. The efficiency of multiphase TiO$_2$
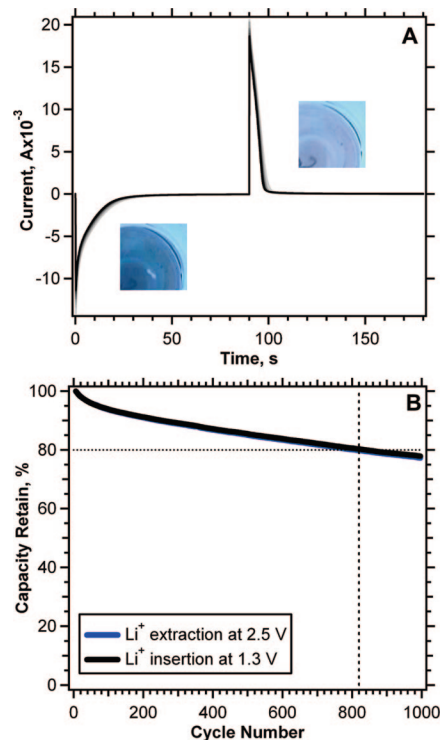

Figure 11. Potential step chronoamperometric cycling of mesoporous TiO$_2$(B) film, thickness 0.7 μm: (A) lithium extraction and insertion profile (1000 cycles), with the color changes of the electrode; (B) cycle stability during 1000 subsequent cycles.
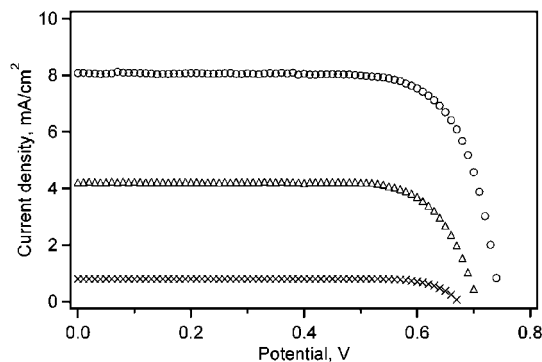

Figure 12. Current−voltage curves of amorphous TiO$_2$−anatase (crosses), TiO$_2$(B)−anatase (triangles), and pure anatase (circles) mesoporous thin films at 1 Sun intensity. The films have approximately the same layer thickness and dye adsorption capacity.

films in dye sensitized solar cells increases in the series: anatase/amorphous TiO$_2$ < anatase/TiO$_2$(B) < anatase.

Supporting Information Available: Current−voltage curves and short-circuit current characteristics of amorphous TiO$_2$, TiO$_2$(B)−anatase, and pure anatase mesoporous thin films (PDF). This material is available free of charge via the Internet at http://pubs.acs.org.

CM801819Q